SURFACE STRUCTURE

Stoichiometric reconstruction of the Al$_2$O$_3$(0001) surface

Johanna I. Hütner[1]†, Andrea Conti[1]†, David Kugler[1], Florian Mittendorfer[1], Georg Kresse[2], Michael Schmid[1], Ulrike Diebold[1], Jan Balajka[1]*

Macroscopic properties of materials stem from fundamental atomic-scale details, yet for insulators, resolving surface structures remains a challenge. We imaged the basal (0001) plane of α–aluminum oxide (α-Al$_2$O$_3$) using noncontact atomic force microscopy with an atomically defined tip apex. The surface formed a complex ($\sqrt{31} \times \sqrt{31}$)$R\pm9°$ reconstruction. The lateral positions of the individual oxygen and aluminum surface atoms come directly from experiment; we determined with computational modeling how these connect to the underlying crystal bulk. Before the restructuring, the surface Al atoms assume an unfavorable, threefold planar coordination; the reconstruction allows a rehybridization with subsurface O that leads to a substantial energy gain. The reconstructed surface remains stoichiometric, Al$_2$O$_3$.

Although the surface structures of many materials have been established with atomic precision, wide-bandgap insulators have proven more difficult to image because of the limited applicability of experimental techniques that rely on charged particles. A prototypical example is α–aluminum oxide (α-Al$_2$O$_3$; corundum or sapphire), an insulator with high dielectric strength, mechanical hardness, chemical and thermal resistance, and excellent optical properties. Alumina (Al$_2$O$_3$) is commonly used as an inert and nonreducible support for heterogeneous catalysis (*1*) and in microelectronics. Al$_2$O$_3$ is also an important model system for naturally occurring minerals, such as aluminosilicate clays (*2*), and is thought to be efficient in nucleating ice in clouds, affecting weather and climate (*3*).

The surface of Al$_2$O$_3$ has long been known to rearrange when provided enough thermal energy, and the first observation of a stable ($\sqrt{31} \times \sqrt{31}$)$R\pm9°$ surface reconstruction was already made in the late 1960s (*4*, *5*). Since then, many research groups have tried to elucidate the details of Al$_2$O$_3$ surfaces using diffraction (*6–8*), spectroscopy (*9*, *10*), noncontact atomic force microscopy (nc-AFM) (*11–13*), and computational modeling (*14*). A commonly accepted atomic model of the ($\sqrt{31} \times \sqrt{31}$)$R\pm9°$ reconstruction consists of one or two metallic aluminum (Al) layers at the top (*6*, *7*, *13*), supposedly created by desorption of oxygen (O) from the outermost layers upon high-temperature annealing in ultrahigh vacuum (UHV). According to x-ray diffraction (XRD) experiments (*7*), the Al layers are rotated relative to the underlying bulk, which gives rise to a coincidence pattern with a ($\sqrt{31} \times \sqrt{31}$)$R\pm9°$ periodicity. However, there is no experimental evidence that the alleged metallic surface of this perfect insulator is conducting (*15*). Moreover, a surface with metallic Al is expected to be unstable. The Al evaporation rate is high at the temperatures at which the reconstruction forms (>1000°C), and an Al surface should be reactive in air, which is in conflict with experimental observations (*6–8*).

We used nc-AFM based on the stiff qPlus force sensor (*16*) to overcome the inherent difficulty of imaging the surface of a wide-gap insulator with atomic resolution. Crucially, the atomically controlled tip apex (*17*) provided chemical identification of individual surface atoms through variations in image contrast. We then used the nc-AFM images to extract the atomic positions of the α-Al$_2$O$_3$(0001)–($\sqrt{31} \times \sqrt{31}$)$R\pm9°$ surface. The determination of the subsurface layers was assisted by means of density functional theory (DFT) combined with machine-learned force fields (MLFFs). We found that the composition of the extensively reconstructed layer was actually very close to that of the bulk, but the surface energy was much lowered compared with a simple bulk truncation. The reconstruction was driven by changing the coordination of surface cations to configurations that allow bonding to subsurface O atoms.

Noncontact AFM resolved individual Al and O atoms of the reconstructed surface

The α-Al$_2$O$_3$(0001) samples formed the ($\sqrt{31} \times \sqrt{31}$)$R\pm9°$ reconstruction upon annealing in UHV or 10^{-6} mbar O$_2$ to 1000°C. No further changes were observed at higher temperatures (up to 1300°C). Annealing above 1000°C removed any surface contamination, as evidenced with x-ray photoelectron spectroscopy (XPS) (fig. S1). nc-AFM images of the $\sqrt{31}$-reconstructed surface (Fig. 1) demonstrate structural diversity of the reconstruction unit cell, including characteristic triangular (Fig. 1A, green) and hexagonal (Fig. 1A, yellow) features, observed previously by Lauritsen *et al.* (*13*). Some triangular regions contain a bright defect in the center (Fig. 1A, dashed circles), which we identified as a surface Al vacancy. The $\sqrt{31}$ periodicity and the 9° rotational alignment from the bulk lattice are evident in reciprocal space in the fast Fourier transform (FFT) of the AFM image as well as the low-energy electron diffraction (LEED) pattern of the reconstructed surface (Fig. 1B). LEED simultaneously detected both rotational domains of the reconstructed surface, leading to a superposition of two diffraction patterns rotated by ±9°.

Individual surface atoms can be identified chemically when the apex of the AFM tip is controlled and known. Using a CuOx-terminated tip, introduced by Mönig and colleagues (*17*, *18*), resulted in a drastic change in image contrast compared with the more commonly used metallic and CO-terminated tips (fig. S2). For an O-terminated tip, repulsion from the surface O atom locally increased the oscillation frequency (Fig. 1A and C, bright maxima), whereas the attraction between the tip and the surface Al downshifted the frequency (Fig. 1A and C, dark minima). The lateral positions of individual surface Al and O atoms could be determined on the basis of the local frequency variations (Fig. 1D). The atomically resolved nc-AFM image in Fig. 1C revealed a variety of local arrangements. Near the corners of the unit cell, the bright O atoms form a honeycomb pattern. Surface O atoms surrounding Al atoms in distorted squares and triangles are shown in Fig. 1D on top of a symmetry-averaged image to reduce noise and tip asymmetry (fig. S3).

DFT calculations accelerated with machine learning identified the stable structure

The experimental nc-AFM images provided the lateral positions of the surface Al$_s$ and O$_s$ atoms. To create a complete three-dimensional model of the Al$_2$O$_3$(0001)–($\sqrt{31} \times \sqrt{31}$)$R\pm9°$ reconstruction, the interface layers that connect the experimentally accessible surface to the bulk corundum structure needed to be determined. The squares and triangles of surface O$_s$ atoms with an Al$_s$ at the center (Fig. 1) are the same structural motifs as in ultrathin alumina films (*19*, *20*). All of these structures exhibit a distorted hexagonal Al$_s$ lattice with Al–Al distances of ≈3.04 Å. On the basis of this similarity, the building blocks of the $\sqrt{31}$ reconstruction were identified as Al$_s$ in tetrahedral or pyramidal coordination to the surrounding O$_s$ atoms in the surface and one interface O$_i$ atom located below each Al$_s$ (Fig. 2B, inset). These interfacial O$_i$ atoms form the apices of downward pointing tetrahedra and pyramids (truncated octahedra). The number of O$_i$ atoms thus should be identical to the number of Al$_s$ atoms (76 per $\sqrt{31}$-unit cell) determined from AFM.
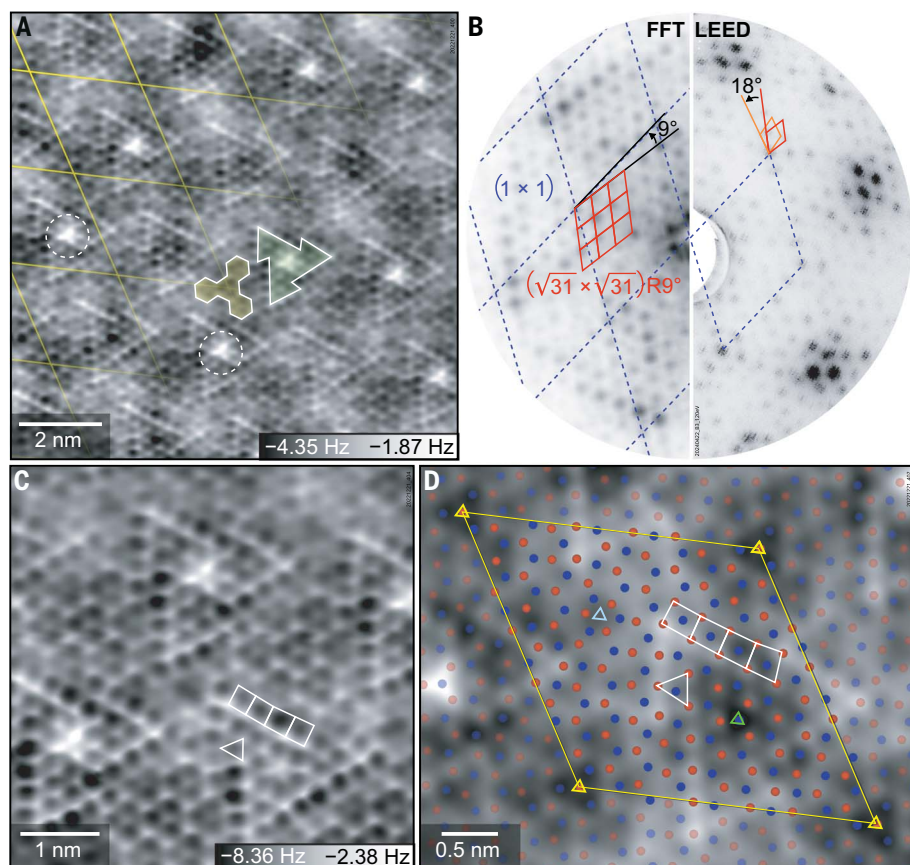
Such arrangement of the O$_i$ atoms resulted in a lower density of the interfacial O layer

[1]Institute of Applied Physics, TU Wien, 1040 Vienna, Austria. [2]Faculty of Physics, University of Vienna, 1090 Vienna, Austria.
*Corresponding author. Email: jan.balajka@tuwien.ac.at
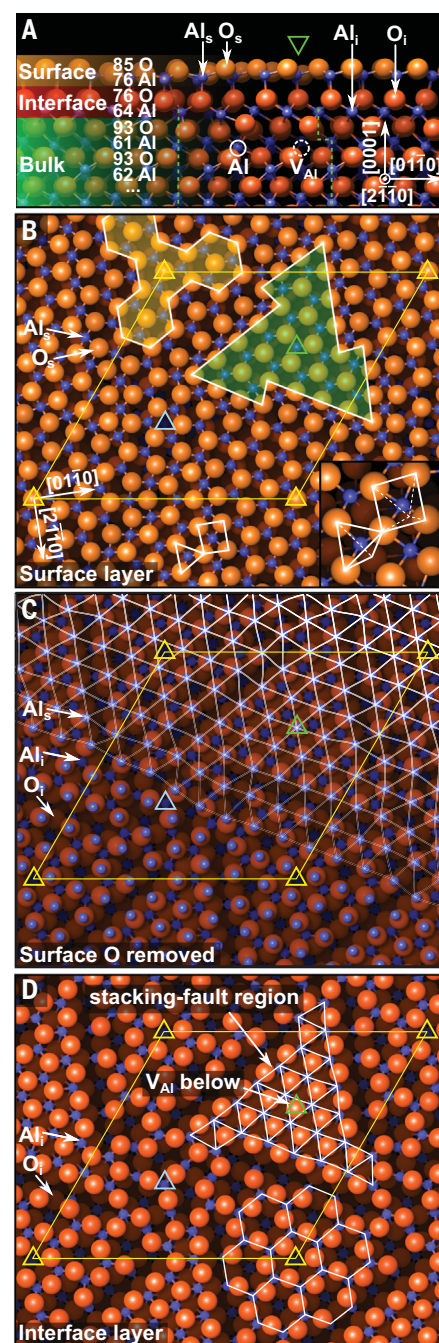†These authors contributed equally to this work.

Fig. 1. The ($\sqrt{31} \times \sqrt{31}$)$R\pm9°$ reconstructed surface of Al$_2$O$_3$(0001). (**A** and **C**) nc-AFM images acquired at 4.7 K with a CuOx terminated tip at constant height. Oscillation amplitudes of (A) 500 pm and (C) 300 pm and a sample bias of −2.7 V were applied. Square and triangular arrangements of the surface O atoms are indicated with white lines, characteristic features are indicated in yellow and green, and two defects (surface Al vacancies) are indicated with white dashed circles. A yellow grid indicates the $\sqrt{31}$ reconstruction lattice. (**B**) FFT of the AFM image in (A) and LEED pattern recorded at 120 eV. A blue dashed grid indicates the bulk (1 × 1) reciprocal lattice. The rotational domains (±9°) of the reconstruction lattice are indicated in red and orange. (**D**) Symmetry-averaged nc-AFM image with atomic positions derived from the maxima and minima in the bandpass-filtered image in fig. S3 (O, red; Al, blue). Colored triangles indicate the threefold symmetry centers.

Fig. 2. Structure model of the Al$_2$O$_3$(0001)– ($\sqrt{31} \times \sqrt{31}$)$R\pm9°$ surface. (**A**) Section view and (**B** to **D**) top views with (C) the O$_s$ removed and (D) all surface atoms removed. The numbers of Al and O atoms per ($\sqrt{31} \times \sqrt{31}$)$R\pm9°$ unit cell are given in each layer in (A). The $\sqrt{31}$ unit cell is indicated with yellow rhombi, and the centers of symmetry are indicated with colored triangles. Characteristic square, triangular, and honeycomb motifs observed in experimental images are indicated. The white triangular grid in (D) indicates the stacking-fault region of the Al$_i$ atoms.

(Fig. 2D) as compared with that of corundum, with 76 instead of 93 O atoms per layer. The O$_i$ atoms would be expected to bind to two or three interfacial Al$_i$ atoms below to complete their coordination. Assuming a near-stoichiometric surface, the number of Al$_i$ atoms should be 62 to 63 per $\sqrt{31}$-unit cell. In the corners of the reconstructed unit cell, the bright surface O$_s$ atoms form an interconnected honeycomb pattern (Fig. 1A, yellow area), suggesting a similar arrangement of the Al$_i$ atoms below (20). The similarity with the honeycomb structure of Al atoms in bulk corundum indicates bulk-like stacking in these areas. The remaining parts of the unit cell (Fig. 1A, green triangular area) exhibit a dense hexagonal arrangement of octahedrally coordinated Al$_i$ atoms with no honeycomb-like brightness modulations.

On the basis of these considerations, initial structure models were created manually and

optimized computationally, and the number of Al and O atoms at the interface were varied to account for the yet unknown stoichiometry. We combined DFT calculations with MLFF to accelerate the search (supplementary materials). More than 100 initial structures were obtained through simulated annealing, and approximately 50 more were created manually and relaxed to test their viability.
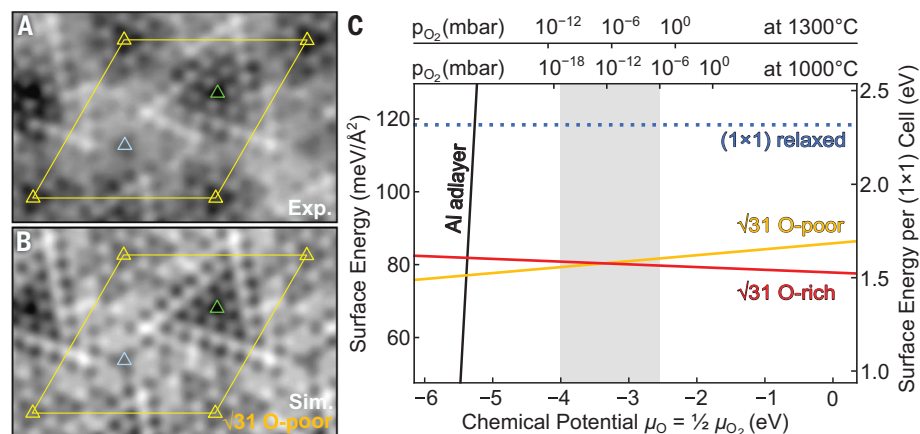
The model of the $\sqrt{31}$ reconstruction shown in Fig. 2 fulfilled two critical structure search criteria simultaneously: the lowest surface energy in the range of relevant O chemical potentials and the best agreement between ex- perimental and simulated AFM images. Consistent with XPS data (fig. S4), the reconstructed surface model is terminated with a layer of O$_s$ protruding above the first layer of Al$_s$ (Fig. 2A). The top view (Fig. 2B) shows the relaxed arrangement of surface atoms, with

only small root-mean-square deviations (0.15 and 0.21 Å for Al$_s$ and O$_s$, respectively) from the positions obtained by means of nc-AFM.

Fig. 3. Stable Al$_2$O$_3$(0001) termination matches experimental AFM. (**A**) Experimental and (**B**) simulated AFM images of the lowest-energy model in Fig. 2. (**C**) Ab initio phase diagram. The surface energies are plotted as a function of the chemical potential of O; the gray stripe highlights the range of experimental conditions. In this range, the O-poor model in Fig. 2 and its O-rich version (with a surface Al vacancy) are nearly isoenergetic.

The distorted hexagonal Al$_s$ lattice is apparent in Fig. 2C, where the O$_s$ atoms were removed. The interface layer (Fig. 2D) consists of two main regions with different arrangements of O$_i$ and Al$_i$ atoms. Near the corners of the $\sqrt{31}$ unit cell, the Al$_i$ atoms are near their bulk positions and form a honeycomb pattern as in the corundum structure, and the O$_i$ atoms form a rather open structure. In the triangular region near the symmetry center (Fig. 2D, green triangle), the O$_i$ and Al$_i$ atoms form a denser, hexagonal lattice. The Al atoms in this region are stacked differently from the usual on-top stacking in corundum (Fig. 2A, dashed green lines), creating a stacking fault. These two regions dominated the contrast of experimental nc-AFM images in Fig. 1, honeycomb (Fig. 1, yellow) and triangular (Fig. 1, green, stacking fault). The complete structure model, including two subsurface layers, is shown in fig. S5. The troughs in the interfacial structure between the stacking-fault and honeycomb regions are consistent with fewer O atoms as compared with bulk corundum.

The high local density of positively charged Al within the stacking-fault region (Fig. 2, B and D) has two consequences. First, the most favorable model has an Al vacancy V_{Al} below the stacking fault in the bulk layer just below the interface (Fig. 2 and fig. S5). Second, high-temperature molecular dynamics simulations suggested that a surface Al atom could be removed from the center of the triangular region. The preference for creating an Al$_s$ vacancy at the (symmetry) center of the stacking-fault region was confirmed with the calculations shown in fig. S6. Upon removal, the three surrounding (undercoordinated) O atoms relaxed upward, causing the bright triangular appearance frequently observed in the nc-AFM images (Fig. 1 and fig. S7).

The structure with a surface Al vacancy at the symmetry center is nearly isoenergetic with the one in Fig. 2 in the range of experimental conditions (Fig. 3C). Coexistence of both defective and nondefective unit cells is thus expected, which is in agreement with experimental nc-AFM images (Fig. 1). The structure in Fig. 2 is only slightly reduced, with a deficit of one O atom per $\sqrt{31}$ reconstruction unit cell ($\sqrt{31}$ O-poor) compared with stoichiometric Al$_2$O$_3$, whereas the structure with the additional Al$_s$ vacancy has a surplus of ½ O atom per $\sqrt{31}$ reconstruction unit cell ($\sqrt{31}$ O-rich). Thus, the coexistence of the two structures at the surface is near stoichiometric, countering the idea that the $\sqrt{31}$ reconstruction should be a reduced surface. In addition to the structure in Fig. 2 and its variant with an Al vacancy, the nc-AFM images revealed slight structural irregularity at the border of the stacking-fault region in some unit cells (for example, fig. S2B, arrow). The deviations from the usual appearance indicate variability at the interface to possibly accommodate any remaining nonstoichiometry, whereas the surface layer remains unchanged.

Simulated AFM reproduces experimental contrast

For a direct comparison with the experimental nc-AFM images, we generated simulated AFM images of the structure models. The simulated image of the stable structure in Fig. 2 shows a strong correspondence with the experimental image (Fig. 3, A and B). To demonstrate the sensitivity of this method, a simulated AFM image of the lowest-energy structure with the same stoichiometry but a qualitatively different arrangement of the interface atoms is presented in fig. S8. The differences in the structures are relatively minor and limited to

the boundary of the stacking-fault region in the interface layer, yet the visual agreement with the experimental image is noticeably worse. The sensitivity of the simulated AFM images is not limited to high-contrast areas but equally applies to the low-contrast region near the light-blue triangle in Figs. 2 and 3. AFM simulations thus serve as a valuable tool for verifying the structural models.

The $\sqrt{31}$ reconstructed surface is strongly favored over other structures

The relative stabilities of selected structure models are compared in an ab initio phase diagram in Fig. 3C. The models with and without a surface Al vacancy (Fig. 3C, red and yellow lines, respectively) exhibit the lowest surface energy over a wide range of O chemical potentials (defined in the supplementary materials). The previously proposed Al adlayer model (Fig. 3C, solid black line) (13) is extremely unfavorable except at unrealistically low O chemical potentials (<−5 eV). Compared with the $\sqrt{31}$ reconstruction, the unreconstructed, relaxed (1 × 1) surface is also very unfavorable (almost 50% higher in energy).

The structure model agrees with existing experimental data

The structure of the reconstructed Al$_2$O$_3$(0001) surface determined in this work is distinctly different from that of previously suggested models. However, it agrees with existing experimental data. Our AFM images reproduced previous measurements (11, 13), albeit with higher resolution thanks to the stiff qPlus nc-AFM sensor and chemical sensitivity based on the controlled tip apex. The new model, with two reconstructed Al and O atomic layers (Fig. 2), corroborated the presence of two distorted hexagonal Al planes with interatomic distances of ≈3.03 Å atop the corundum bulk, established by Renaud et al. through surface x-ray diffraction (SXRD) experiments (7). Similarly, the model proposed here contains a layer with a nearly hexagonal lattice of surface Al$_s$ atoms (Fig. 2C) with an almost identical average Al–Al in-plane distance of 3.04 Å and a second Al plane with a similar lattice in the stacking-fault region (Fig. 2D). Complementing XRD, nc-AFM—particularly with an O-terminated tip—is suited to detect O atoms at the surface and directly visualize the intricate local atomic configurations.

The reconstruction is stabilized by increasing Al coordination

Why does such a restructuring occur on the basal plane of a seemingly simple binary oxide? The bulk lattice of corundum is composed of hexagonal, close-packed, (0001)-oriented O layers separated by pairs of laterally shifted hexagonal Al planes, resulting in a stack of stoichiometric (Al–O$_3$–Al)$_n$ units. Each Al is

coordinated to three O atoms from the layers above and three below (fig. S9A). A cut along (0001) between the Al planes of two adjacent Al–O$_3$–Al units creates a nonpolar surface, the standard model of the (1 × 1) termination. DFT calculations show that the undercoordinated terminal Al atoms on the (1 × 1) surface strongly relax inward by 0.7 Å, resulting in an almost coplanar geometry (Al is only 0.14 Å above the O layer) (fig. S9B). In the relaxed geometry, the short Al–O bond length of 1.69 Å (compared with the $\sqrt{31}$ structure in fig. S10) leads to compressive stress in the surface layer, with an energy cost of ≈0.1 eV per (1 × 1) cell. The strain energy alone cannot explain the difference in surface energies of 0.75 eV per (1 × 1) cell between the relaxed (1 × 1) surface and the reconstruction (Fig. 3C).

The nearly threefold-planar coordination of the topmost Al of the (1 × 1) termination implies that their p_z orbitals cannot bind to any O neighbor, as also indicated by the projected density of states (fig. S11). The energy cost for a nonbonding Al p_z orbital can be estimated by comparison with threefold-planar aluminum trihalide molecules and their dimers: These molecules achieve a distorted tetrahedral coordination by dimerization (fig. S12, inset). The energy gain upon dimerization is 1.11 eV per Al for AlF$_3$ → Al$_2$F$_6$ and 0.64 eV for AlCl$_3$ → Al$_2$Cl$_6$ (21). Because Al prefers to bind to electronegative elements and the electronegativity of O is between that of F and Cl, we estimate that the energy cost of a nonbonding Al p_z is around 0.8 eV relative to a coordination in which all Al 3s and 3p orbitals take part in bonding (fig. S12).

Converting the standard model of the (1 × 1) surface to any structure where the surface Al atoms have at least tetrahedral coordination (such as the $\sqrt{31}$ reconstruction) avoids one nonbonding Al p_z orbital per (1 × 1) cell. The estimated ≈0.8 eV energy gain per (1 × 1) cell explains the magnitude of the surface energy difference upon reconstruction. The tetrahedral or pyramidal coordination of the surface Al atoms requires an in-plane expansion of the lattice at the surface. The complex $\sqrt{31}$ reconstruction is the result of fitting this expanded surface layer onto the corundum bulk structure.

The Al$_2$O$_3$(0001) surface is substantially stabilized by adopting the $\sqrt{31}$ reconstruction, and recent experimental evidence (8) shows that this structure is stable at all attainable O chemical potentials. The basal planes of other corundum oxides such as chromium oxide (Cr$_2$O$_3$) (22), vanadium oxide (V$_2$O$_3$) (23), and hematite (Fe$_2$O$_3$) (24) show a tendency to reconstruct, and a striking resemblance is evident between reconstructed Al$_2$O$_3$(0001) and hematite Fe$_2$O$_3$(0001) (25). This similarity suggests a unified mechanism that causes reconstructions of oxide surfaces by avoiding undercoordinated metal cations and creating an O-terminated surface. Our work demonstrates that reduced or over-oxidized surfaces of materials with a large bandgap are unfavorable.

REFERENCES AND NOTES

1. F. Rascón, R. Wischert, C. Copéret, *Chem. Sci.* **2**, 1449–1456 (2011).
2. P. J. Eng *et al.*, *Science* **288**, 1029–1033 (2000).
3. A. Soni, G. N. Patey, *J. Phys. Chem. C Nanomater. Interfaces* **123**, 26424–26431 (2019).
4. C. C. Chang, *J. Appl. Phys.* **39**, 5570–5573 (1968).
5. T. M. French, G. A. Somorjai, *J. Phys. Chem.* **74**, 2489–2495 (1970).
6. M. Gautier *et al.*, *J. Am. Ceram. Soc.* **77**, 323–334 (1994).
7. G. Renaud, B. Villette, I. Vilfan, A. Bourret, *Phys. Rev. Lett.* **73**, 1825–1828 (1994).
8. S. Smink, L. N. Majer, H. Boschker, J. Mannhart, W. Braun, *Adv. Mater.* **36**, e2312899 (2024).
9. M. Gautier, J. P. Duraud, L. Pham Van, M. J. Guittet, *Surf. Sci.* **250**, 71–80 (1991).
10. E. Gillet, B. Ealet, *Surf. Sci.* **273**, 427–436 (1992).
11. C. Barth, M. Reichling, *Nature* **414**, 54–57 (2001).
12. J. Wang, A. Howard, R. G. Egdell, J. B. Pethica, J. S. Foord, *Surf. Sci.* **515**, 337–343 (2002).
13. J. V. Lauritsen *et al.*, *Phys. Rev. Lett.* **103**, 076103 (2009).
14. E. A. A. Jarvis, E. A. Carter, *J. Phys. Chem. B* **105**, 4045–4052 (2001).
15. A. Chame *et al.*, *Int. J. Mod. Phys. B* **11**, 3657–3671 (1997).
16. F. J. Giessibl, *Rev. Sci. Instrum.* **90**, 011101 (2019).
17. B. Schulze Lammers *et al.*, *Nanoscale* **13**, 13617–13623 (2021).
18. P. Wiesener *et al.*, *ACS Nano* **18**, 21948–21956 (2024).
19. G. Kresse *et al.*, *Science* **308**, 1440–1442 (2005).
20. M. Schmid *et al.*, *Phys. Rev. Lett.* **99**, 196104 (2007).
21. M. W. Chase, *NIST-JANAF Thermochemical Tables* (American Chemical Society, 1998).
22. O. Bikondoa *et al.*, *Phys. Rev. B Condens. Matter Mater. Phys.* **81**, 205439 (2010).
23. G. Kresse, S. Surnev, J. Schoiswohl, F. P. Netzer, *Surf. Sci.* **555**, 118–134 (2004).
24. J. Redondo *et al.*, *J. Phys. Chem. C Nanomater. Interfaces* **123**, 14312–14318 (2019).
25. J. Redondo *et al.*, *Adv. Mater. Interfaces* **10**, 2300602 (2023).

SUPPLEMENTARY MATERIALS

science.org/doi/10.1126/science.adq4744
Materials and Methods
Figs. S1 to S14
References (26–39)
Structure Models S1 and S2

Submitted 15 May 2024; accepted 15 July 2024
10.1126/science.adq4744